The Company of
Biologists

RESEARCH ARTICLE

Cancer cells in the tumor core exhibit spatially coordinated migration patterns

Ralitza Staneva[1,2,‡], Fatima El Marjou[1], Jorge Barbazan[1], Denis Krndija[1], Sophie Richon[1], Andrew G. Clark[1,*,‡] and Danijela Matic Vignjevic[1,*]

ABSTRACT

In the early stages of metastasis, cancer cells exit the primary tumor and enter the vasculature. Although most studies have focused on the tumor invasive front, cancer cells from the tumor core can also potentially metastasize. To address cell motility in the tumor core, we imaged tumor explants from spontaneously forming tumors in mice in real time using long-term two-photon microscopy. Cancer cells in the tumor core are remarkably dynamic and exhibit correlated migration patterns, giving rise to local 'currents' and large-scale tissue dynamics. Although cells exhibit stop-and-start migration with intermittent pauses, pausing does not appear to be required during division. Use of pharmacological inhibitors indicates that migration patterns in tumors are actively driven by the actin cytoskeleton. Under these conditions, we also observed a relationship between migration speed and correlation length, suggesting that cells in tumors are near a jamming transition. Our study provides new insight into the dynamics of cancer cells in the tumor core, opening new avenues of research in understanding the migratory properties of cancer cells and later metastasis.

This article has an associated First Person interview with the first author of the paper.

KEY WORDS: Cancer cell migration, Tumor explant, Tissue imaging, Collective behavior

INTRODUCTION

Cell migration is an essential process in the development and homeostasis of multicellular organisms. In pathological conditions such as metastatic cancer, cells acquire an upregulated capacity for migration (Lambert et al., 2017). During the progression of carcinoma metastasis, cancer cells breach the surrounding basement membrane and invade into the stroma, which is composed of extracellular matrix (ECM) and stromal cells (Chambers et al., 2002). In the stroma, features of the microenvironment that modulate the modes of cancer cell migration, such as collagen density and alignment, have been described (Provenzano et al., 2006, 2008; Gligorijevic et al., 2014). Invading cells migrate through the stroma to reach blood or lymph vessels, which are also embedded in the stromal ECM network. Interestingly, it has recently been shown that vascular escape can also occur in deep regions of tumors and not only in the invasive front (Deryugina and Kiosses, 2017).

[1]Institut Curie, PSL Research University, CNRS, UMR 144 - Cell Biology and Cancer, 75005 Paris, France. [2]University Paris Descartes, 12 rue de l'Ecole de Médecine, 75006 Paris, France.
*These authors contributed equally to this work

‡Authors for correspondence (ralitza.staneva@curie.fr; andrew.clark@curie.fr)

R.S., 0000-0002-2125-6326; A.G.C., 0000-0003-3712-4931

Most solid tumors, including colorectal cancer, are composed of a central differentiated core region – or tumor bulk – and an invasive front forming the interface between tumor and stromal tissue (Vignjevic et al., 2007; Clark and Vignjevic, 2015). The invasive front is widely characterized in terms of cell morphology and molecular composition (Prall, 2007). Intravital imaging has uncovered a large diversity of cancer cell migration modes at the invasive front, ranging from collective behaviors to single cell migration (Friedl and Wolf, 2010; Clark and Vignjevic, 2015). In contrast, the dynamics of the tumor core are far less understood, and we still lack precise details of single-cell dynamics and migration patterns within the tumor core. To address this, we studied the behavior of cancer cells in densely packed regions in the tumor core using a mouse model of genetically induced aggressive intestinal carcinoma.

In this model, tumors spontaneously arise in the intestine and metastasize to the lymph nodes, peritoneum and liver (Chanrion et al., 2014), reflecting the heterogeneity and growth timescales of naturally occurring tumors. Due to the inaccessibility of deep regions of intestinal tumors for intravital imaging, we imaged tumor explant slices using two-photon excitation microscopy (Staneva et al., 2018). Using this model, we investigated the migratory behavior of cancer cells in the tumor core of spontaneously developing intestinal tumors and found that cancer cells in the tumor core are not stationary. On the contrary, cells in the tumor core exhibit coordinated migratory patterns that give rise to large-scale tissue dynamics.

RESULTS

Tumor explants recapitulate tissue properties found *in vivo*

To study the growth and migratory behaviors of cancer cells in spontaneously developing tumors, we used the NICD/p53$^{-/-}$ tumor model (Chanrion et al., 2014). In this mouse model, the formation of invasive carcinoma is driven by the expression of a conditionally activated receptor Notch1 (NICD) and the deletion of the tumor suppressor p53 (also known as TP53) in the intestinal epithelium following tamoxifen injection. Expression of nucleus-targeted GFP allows visualization and tracking of cancer cell nuclei. In addition, crossing these mice with mT/mG reporter mice (Muzumdar et al., 2007) allows visualization of cell membranes.

In order to analyze cancer cell migration in deep tumor core areas, we performed live imaging on thick tumor explant slices (Staneva et al., 2018) (Fig. S1A). Tissue slices were ∼250 µm thick, and imaging was performed near the center of the slices, ∼60 µm away from the underlying filter. Using this method, we were able to culture and image tumor explants for up to 40 h (Movie 1). Explant culture and two-photon imaging allows for analysis of cell growth and migration in deep tumor areas that are inaccessible to intravital imaging techniques. In NICD/p53$^{-/-}$ tumors, the invasive front comprises the collagen-rich tumor capsule, cancer cells colonizing this capsule and regions just beneath the capsule (Fig. 1A, inset 1; Fig. S1B, upper panels). The tumor capsule is composed of
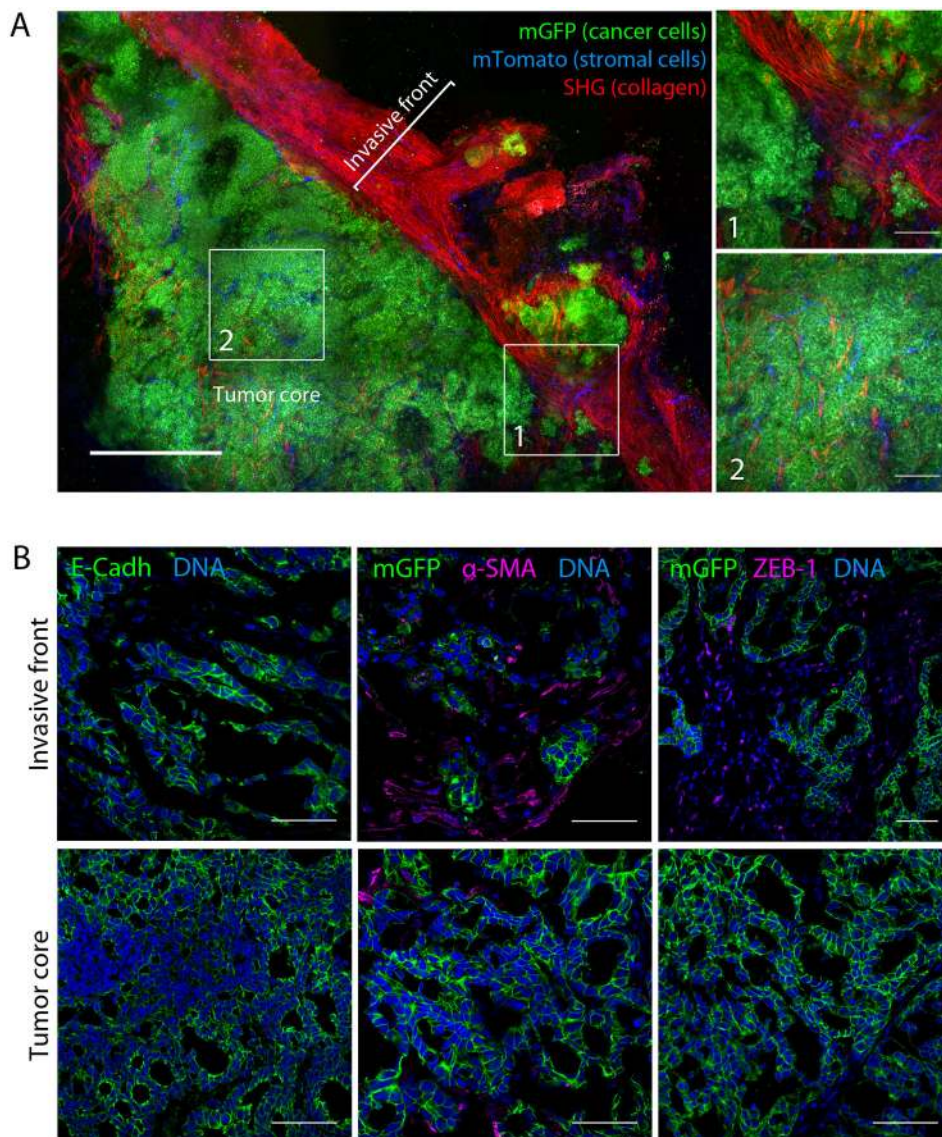
Fig. 1. Architecture of the tumor core in NICD/p53$^{-/-}$ carcinoma. (A) Left: stitched image of a large tumor area showing the tumor core and the invasive front in a NICD/Tom/p53$^{-/-}$ mouse, with cancer cells expressing membrane-targeted GFP (mGFP, green) and stromal cells expressing membrane-targeted Tomato (mTomato, blue). Collagen is visualized through its intrinsic optical properties [second harmonic generation (SHG), red]. Scale bar: 500 μm. Right: boxed region 1 (invasive front) and 2 (tumor core) from the stitched image are magnified. Scale bars: 100 μm. (B) Staining for E-cadherin (E-Cadh), α-smooth muscle actin (α-SMA), and ZEB-1 in invasive front and tumor core regions. Scale bars: 50 μm.

fibrillar collagen bundles aligned parallel to the tumor edge and interpenetrated by blood vessels. Present at the invasive front are E-cadherin-positive cancer cell clusters (Fig. 1B, upper left panel), as well as single cells. Single cells are positive for smooth muscle actin (α-SMA, also known as ACTA2) and ZEB-1 (Fig. 1B, upper middle and right panels); previous work with this model has shown that a subset of ZEB-1-positive cells at the invasive front are of epithelial origin and have undergone an epithelial-to-mesenchymal transition (EMT) (Chanrion et al., 2014). Deeper in the interior of the tumor is the tumor core, which is composed of densely packed epithelial tumor cells (Fig. 1A, inset 2; Fig. 1B, lower panels; Fig. S1B, lower panels). The tumor core also contains blood vessels, stromal cells and smaller collagen bundles that are less densely packed than in invasive regions (Fig. 1B, lower panels; Fig. S1B, lower panels). The presence of these structures in the tumor core reflects the physiological nature of this model, where tumors and ECM co-evolve on physiological timescales.

To ensure that tumor explants remained viable, we quantified division rates (Fig. S1C–E). In order to compare the proliferation rates of NICD/p53$^{-/-}$ tumors *in vivo* and *ex vivo*, we quantified uptake of the thymidine analog EdU (5-ethynyl-2′-deoxyuridine), which is incorporated during S-phase. We found no significant difference

between proliferation rates *in vivo* and *ex vivo*, at early or later timepoints (Fig. S1C), suggesting that culturing tumors *ex vivo* does not alter their growth rate over the imaging duration. We also quantified the rate of cell division in explants using expression of genetically encoded nuclear GFP to observe cells undergoing mitosis (Fig. S1D). In the first 8 h of imaging, on average 2.7% of cells divided (Fig. S1E) with divisions lasting 45 min–1 h (Fig. S1F).

We observed that tissue architecture was conserved after long-term *ex vivo* culture, as revealed by the maintenance of actin organization and cell–cell junctions and the absence of EMT in the tumor core (Fig. S2A). Cell proliferation was constant throughout the duration of tissue explant culture and in different depths of the tissue (Fig. S2B). Tumor areas with high cell death increased ∼3-fold after 24 h of incubation (Fig. S2C); regions with high cell death were heterogeneously distributed in the tissue and were not acquired for further investigation. Cell death was apparent in both epithelial tumor cells and stromal cells in the tumor core (Fig. S2D). We also found that hypoxia levels decreased during culture (Fig. S2E; see Discussion). Together, these data show that tumor explants recapitulate tissue properties found *in vivo* and thus can be used as a model system to investigate cell behaviors in the tumor core, with limitations for some specific questions (see Discussion).

Cells in tumor core display heterogeneous speeds and persistence

To analyze migration dynamics in the tumor core, we manually tracked a random selection of tumor cells (Fig. 2A; Movie 2). We observed a wide range of migration persistence, a measure of the straightness of trajectories (Fig. 2B). Approximately 75% of cells migrated with moderate persistence, between 0.10 and 0.70; ~20% of cells displayed highly persistent migration, with persistence >0.70 (Fig. 2B). To further investigate directional migration, we calculated the average mean squared displacement (MSD). For moderately persistent cells, the MSD increased with respect to time with an exponent of ~1.38 (Fig. 2C, left), while highly persistent cells had an MSD versus time exponent of ~1.86 (Fig. 2C, right), further suggesting that this subset of cells migrate in a highly directional manner. We found that mean instantaneous speed was normally distributed around a mean of ~3.7 μm/h and was constant

over more than 20 h of imaging (Fig. 2D,E). These speeds were within the range of speeds previously found using intravital imaging in several mouse models (Weigelin et al., 2012; Patsialou et al., 2013; Gligorijevic et al., 2014; Clark and Vignjevic, 2015). Most cells (80%) migrated between 1.6 and 4.8 μm/h, corresponding to 0.2–0.6 nuclear diameters per hour (ND/h), with 3% slower than 0.2 ND/h and 17% faster than 0.6 ND/h (Fig. 2D). Most cells reached a maximum instantaneous speed of ~10 μm/h (Fig. 2F). To determine whether cells exhibited any migration bias toward the oxygenated atmosphere above the filter or toward the growth factor-rich medium below the filter, we tracked a subset of cells in 3D (Fig. S3A–D). We found that both mean migration velocity and net cell displacement were distributed around zero in the x, y and z dimensions, suggesting no directional bias during migration (Fig. S3A,B). Moreover, instantaneous and effective speeds were similar in x, y and z directions, indicating that cell displacements
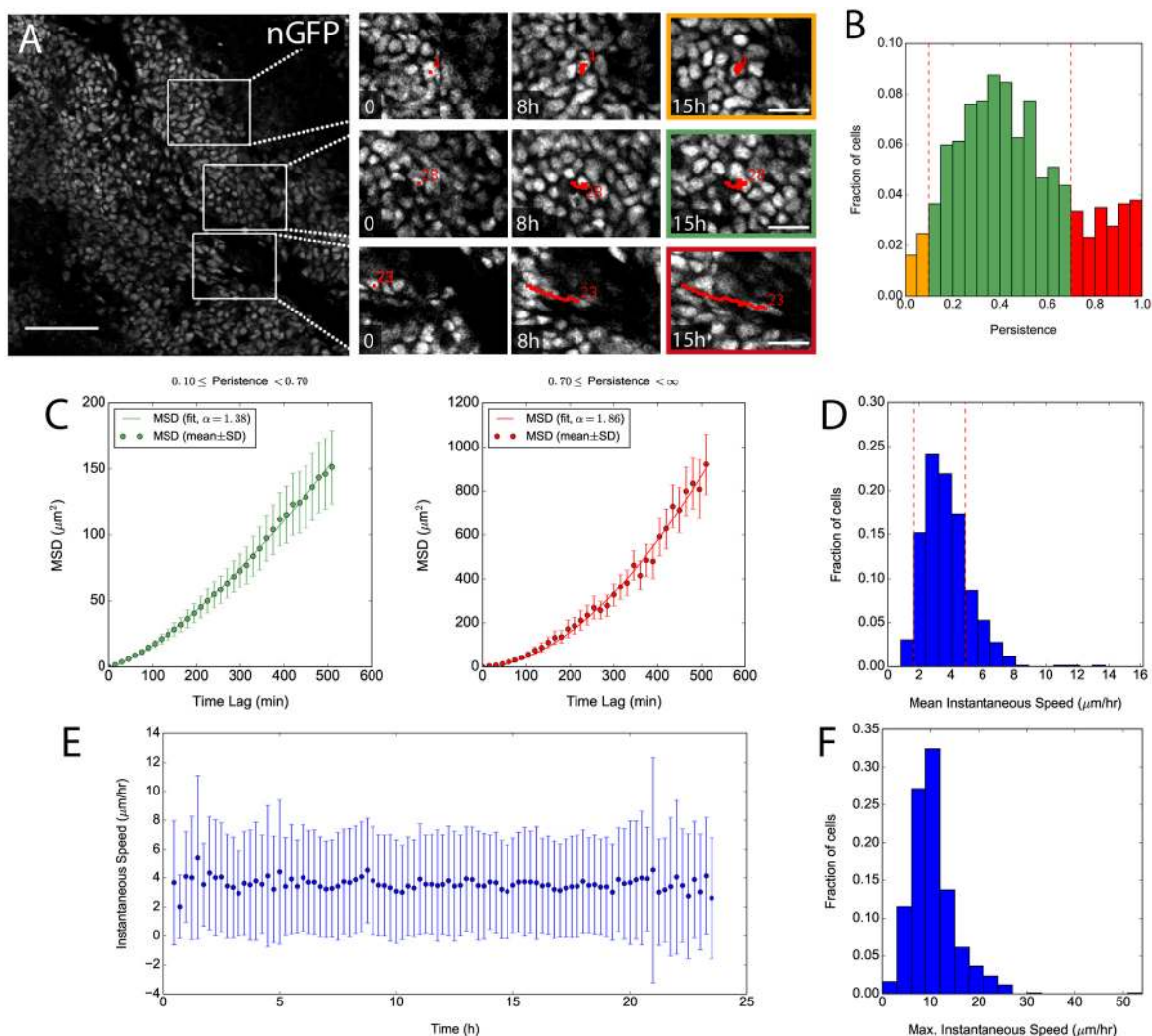

Fig. 2. Cells in NICD/p53$^{-/-}$ carcinoma are motile and display a range of speeds and persistence. (A) Migration patterns of NICD/p53$^{-/-}$ cells. Left panel: z-slice of NICD/p53$^{-/-}$ tumor. Boxed regions are magnified in right panels as indicated. Scale bar: 100 μm. Right panels: NICD/p53$^{-/-}$ cell nuclei were tracked for 15 h. Color frames indicate low persistence (0.04; orange), medium persistence (0.39; green) and high persistence (0.87; red). Time in hours. Scale bars: 30 μm. Red numbers indicate track ID numbers. (B) Histogram of persistence values from tracked cells. The red dotted lines indicate borders between cells with low (<0.1; orange), medium (0.1–0.7; green) or high (>0.7; red) persistence. (C) Average mean squared displacement (MSD) plots for cells with medium (left, green) or high (right, red) persistence (from B). Dots represent mean±s.d. and lines represent power-law fit with resulting exponent α [n=542 cells (left), 133 (right) for six mice]. (D) Histogram of mean instantaneous speeds of tracked cells. The red dotted lines indicate 0.2 and 0.6 nuclear diameters per hour (ND/h), corresponding to 1.6 and 4.8 μm/h, respectively. (E) Plot of instantaneous speeds (mean±s.d.) from all manually tracked cells over the imaging duration (time in hours). (F) Histogram of maximum instantaneous speeds of tracked cells. For panels B,D–F, n=685 cells for six mice.

were comparable in all dimensions (Fig. S3C,D). In order to estimate the noise in cell trajectories, resulting primarily from tissue deformations, we measured the displacement of collagen fibers in the tumor core (Fig. S3E,F). Collagen fibers exhibited mean displacements of 0.85 μm/h, with speeds substantially below that of migrating cells (Fig. S3G). This suggests that the observed cell migration is not simply a consequence of large-scale tissue deformation. Taken together, these data suggest that tumor cells in the core display a wide range of migration dynamics.

In order to assess whether collagen fibers could influence tumor cell migration, we analyzed cell migration direction with respect to local collagen orientations (Fig. S3H). We did not find any significant bias in migration orientation with respect to collagen orientation (Fig. S3I, J), nor could we detect any correlation between the distance from collagen fibers and cell migration speed or persistence (Fig. S3K,L). These data suggest that in the tumor core, collagen fibers may not influence migration orientation or dynamics.

Tumor cells are not required to stop migrating during cell division

It has been long known that during cell migration, cells exhibit pausing behaviors (Abercrombie et al., 1970). To determine whether cells in the tumor core pause during migration, we straightened the trajectories to make kymographs. Individual kymographs revealed that cells paused intermittently, resulting in various stop-start migration patterns (Fig. 3A). On average, migrating cells were paused 20% of the time (Fig. 3B), pausing once every three hours,

and with most pauses 30–40 min long (Fig. S3M,N). These data suggest that tumor cells in this model exhibit stop-and-start behavior, and that pausing dynamics are consistent over the whole population of tumor cells.

In many single-cell systems, migrating cells must stop in order to divide (Abercrombie et al., 1970), and daughter cells begin migrating only when cell division is complete. To investigate this idea in our model, we tracked mother and daughter cells and produced kymographs of their trajectories (Fig. 3C,D). In only 16.6% of cases (6/36) did the mother cell completely pause during division (Fig. 3D, left; dashed circle), consistent with the pause rates of non-dividing cells. In 83.4% of cases, mother cells continued migrating during division (Fig. 3D, right; full circle). We found no significant difference between instantaneous cell speeds of cells before, during or after division or in the presence of the mitotic inhibitor hydroxyurea (HU; Fig. 3E). Taken together, these data suggest that pauses that happen to occur during division are not more frequent than outside division. Thus, cells can still be displaced during division, and there is no strict requirement for pausing during division in this system.

Tumor cells exhibit coordinated migration patterns
The tumor core is dense but migratory. In in vitro monolayers, dense tissues exhibit collective migration and spatial inhomogeneities (Angelini et al., 2011; Tambe et al., 2011). In order to determine whether such collective behavior also exists in dense and migratory tissues in vivo, we investigated directional correlation in tumor core cell migration (Fig. 4A). For each overlapping time point for two
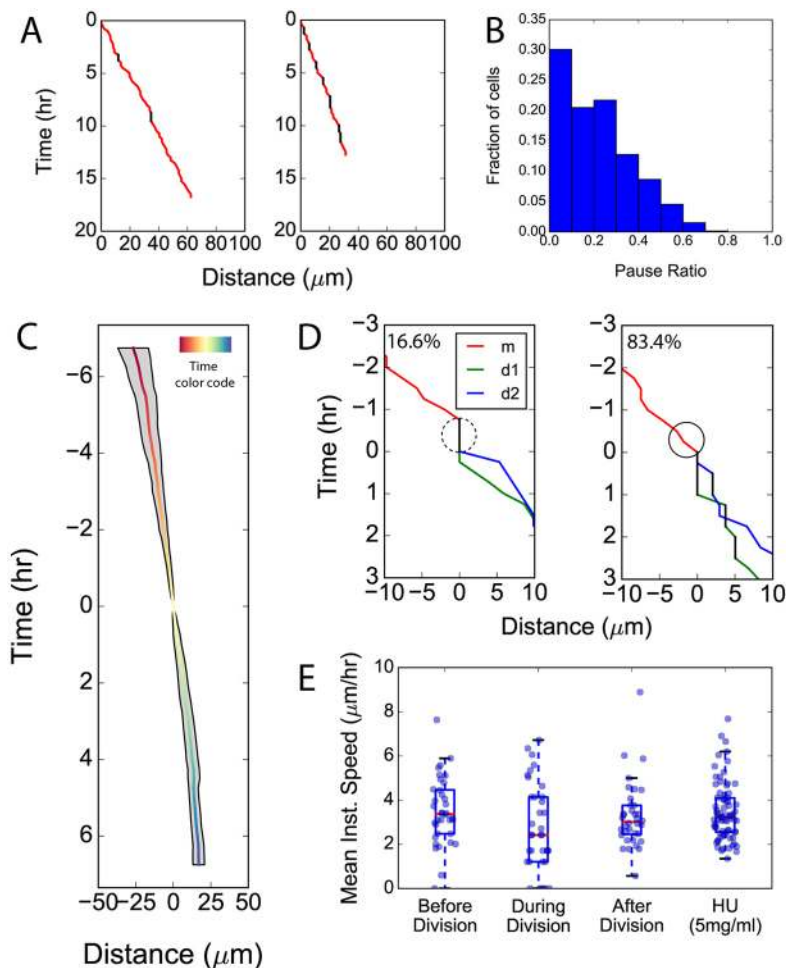

Fig. 3. Pausing during cell division is not required in migrating tumor tissue. (A) Individual kymographs of NICD/ p53$^{-/-}$ carcinoma cell motility showing different pausing behaviors, indicating periods of migration (red) interrupted by pauses (black). Pauses are defined as consecutive periods of ≥30 min with no detectable migration. (B) Histogram of pause ratios for all cell trajectories. Pause ratio is defined as the fraction of the trajectory spent paused (n=685 cells for six mice). (C) Combined kymograph from dividing mother (red to yellow) and daughter (yellow to blue) cell trajectories [n=36 individual division events from three mice; the time color code represents from early time points preceeding division (red) to later time points following division (blue), mean±s.d.]. Kymographs were aligned such that division occurred at time=0 h, distance=0 μm. (D) Kymographs from trajectories of two dividing mother cells (m, red) and their daughter cells (d1, green; d2, blue), demonstrating that some dividing cells pause their migration during division (left, dashed circle), while some cells continue migrating (right, solid circle). (E) Mean instantaneous speeds of cells before, during and after division and following treatment with 5 mg/ml hydroxyurea (HU), a cell division inhibitor. The box represents the interquartile range (IQR; 25–75th percentiles), and the median is indicted. The whiskers extend to the furthest data points below and above the box within the box lower bound−IQR×1.5 and upper bound+IQR×1.5. Data were compared using one-way ANOVA (Kruskal–Wallis test), P-value=0.095 (n=36, 36, 72, 75 cells from three mice each).

cell trajectories, we determined the directional correlation at that time interval, equal to 1 for perfectly parallel migration and −1 for anti-parallel migration (Fig. 4B). We then determined the mean correlation for the trajectories and compared this to the distance between the cells at the start of the trajectory (Fig. 4C). We found that cells close together (<50 μm apart) indeed displayed a directional correlation (∼0.25), and this correlation was lost for cells >250 μm apart (Fig. 4C).

To further investigate the correlation between migration directions, we performed particle image velocimetry (PIV) analysis on the 2D time-lapse images (Fig. 4D; Movie 3). Surprisingly, we found numerous examples of groups of cells exhibiting local migration 'currents' and vortices (Fig. 4D; Movie 3), highlighting the collective nature of cell migration in this system. Although PIV vectors appeared noisier than manual tracks, likely owing to the fact that cells move in and out of different PIV windows, the overall migration correlation and dynamics were strikingly similar between the two techniques (Fig. 4C and Fig. 2D versus Fig. S3O). Taken together, these complementary analyses demonstrate that cells in the tumor core exhibit correlated migration direction.

Active migration in the tumor core is driven by the actin cytoskeleton

We next sought to investigate the mechanisms underlying collective migration in the tumor core. We hypothesized that migration was actively driven by the actin cytoskeleton. To test this, we treated tumor slices with the actin polymerization inhibitor cytochalasin D and compared migration dynamics before and after treatment using PIV

analysis (Fig. 5A). To assess collective migration, we calculated the velocity–velocity correlation, C_{vv}, from the vector fields resulting from PIV data. For each imaging frame, we fit the resulting C_{vv} versus distance, δr, data with an exponential function to determine the correlation length, ζ_{vv} (Fig. 5B) (Garcia et al., 2015). We found that mean migration speed decreased following treatment with cytochalasin D (Fig. 5C), suggesting that the actin cytoskeleton drives active migration in the tumor core. Moreover, cytochalasin D increased the correlation length (Fig. 5D); plotting correlation length versus speed with cytochalasin D treatment, we found that as cell speed increased, correlation length decreased (Fig. 5E). To ensure that cytochalasin D was effective in disrupting actin in tumor slices, we stained samples before and after treatment with phalloidin and observed a substantial change in actin organization in these tissues (Fig. S4A). We performed a similar analysis treating cells with CK-666, an inhibitor of the actin nucleator complex Arp2/3 and para-nitroblebbistatin, a photostable inhibitor of myosin-2 (Fig. S4A, right and Fig. S4B). We observed a decrease in speed with CK-666, but no change in correlation length. Blebbistain, however, did not consistently affect speed or correlation length (Fig. S4C,D). To confirm the PIV results, we performed manual tracking and analyzed cell dynamics before and after treatments with the actomyosin inhibitors and found similar changes in speed, while persistence values were not consistently affected by any of the treatments (Fig. S4C).

Cell movement in intestinal tumors could also be driven in part by pressure fluctuations resulting from cell divisions in the tissue. To test this, we treated tumor slices with the mitotic inhibitors hydroxyurea (HU) and mitomycin C and assessed cell migration
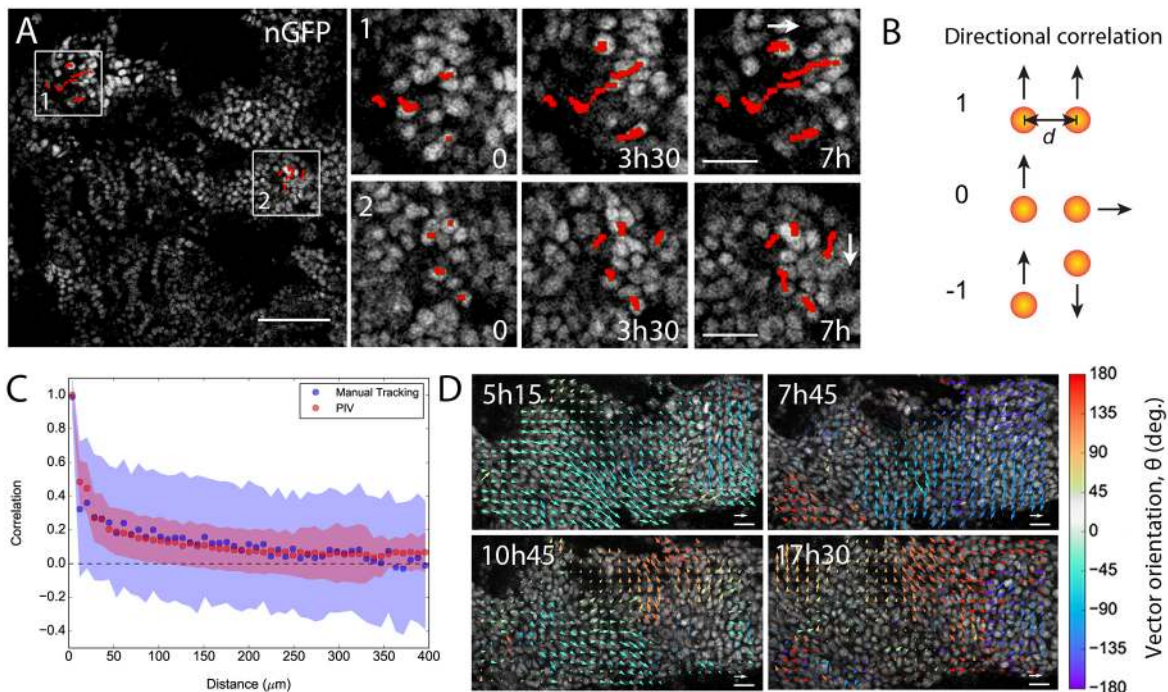

Fig. 4. Tumor core cells exhibit correlated migration patterns. (A) Spatial distribution of migration directions. Left panel: *z*-slice of NICD/p53$^{-/-}$ tumor. Right: boxed regions from left panel are magnified and show similar migration directions for cells in close proximity. White arrows show the main direction of migration for the cells in proximity. Scale bars: 100 μm (left), 30 μm (right). Time in hours. (B) Mean directional correlation is calculated by comparing migration direction for each overlapping time step between different trajectories. Correlation is defined as $(\theta_i - \theta_j)$ for two cells, designated *i* and *j*, at overlapping time point *t*. The mean correlation is determined by averaging the correlation at all overlapping time points, and then compared to the distance between the cells at the start of their trajectories, *d*. (C) Directional correlation versus distance for manually tracked cells and particle image velocimetry (PIV) analysis (mean ±s.d.). The correlation from manual tracking data (blue) was performed as described in B. The correlation from PIV data (red) was determined using the radial auto-correlation function on PIV vector fields (see also Materials and Methods section). (D) Examples of displacement vectors, determined by PIV, overlaid on images of tissue slices. Local currents in cell migration result in larger-scale vortex and swirl patterns. Vector colors indicate direction and lengths indicate magnitude (speeds). Scale vector (white): 6 μm/h. Scale bars: 30 μm. See also Movie 3.
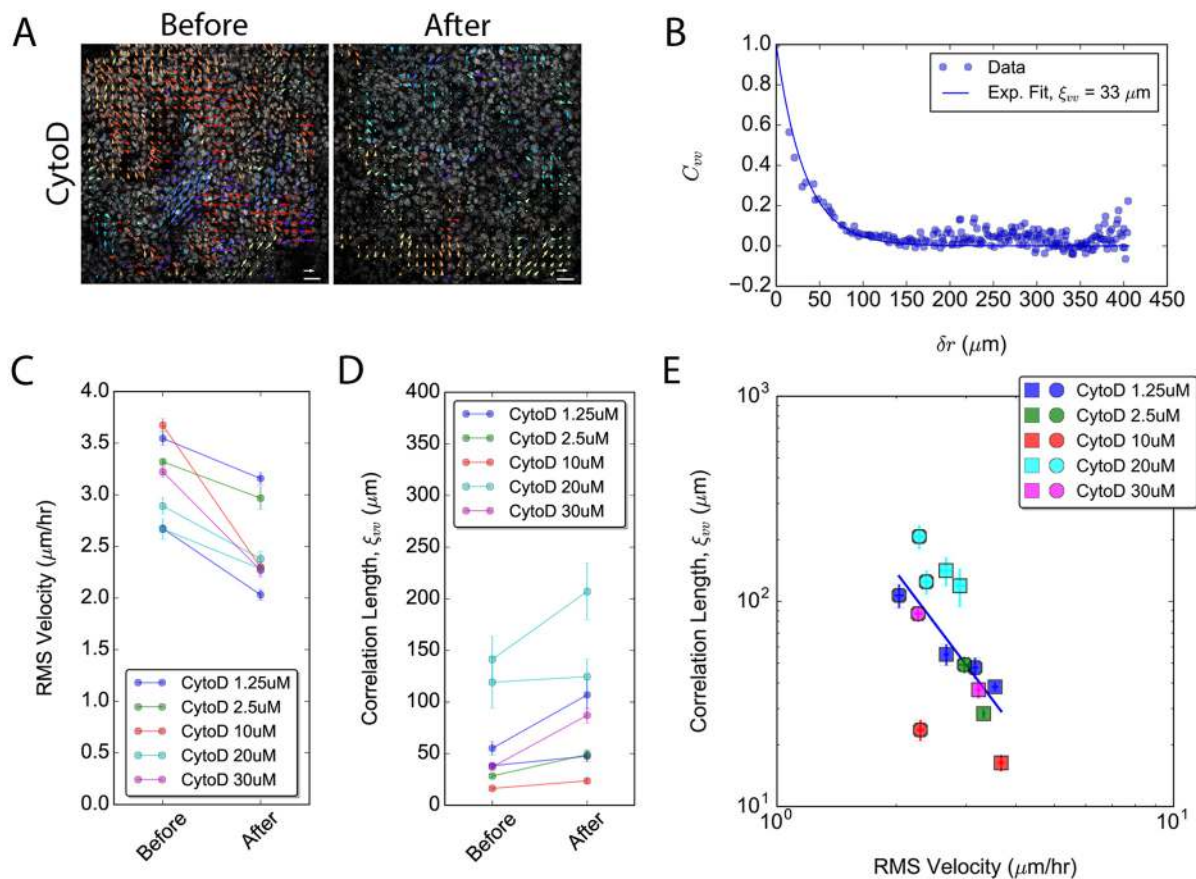
Fig. 5. Active migration in the tumor core is driven by the actin cytoskeleton. (A) Examples of displacement vectors, determined by PIV, overlaid on images of tissue slices for tissues before (with vehicle control) and after treatment with cytochalasin D (CytoD, 20 μM). Vector colors indicate direction and lengths indicate magnitude (speeds). Scale vector (white): 6 μm/h. Scale bars: 30 μm. (B) An example of the radial auto-correlation function to determine velocity–velocity correlation, C_{vv}, over distance (δr), fit with an exponential function to extract the correlation length, ζ_{vv}, for a single PIV frame. (C) Root mean squared (RMS) velocities from PIV analysis before (with vehicle control) and after treatment with cytochalasin D. (D) Correlation lengths extracted from PIV analysis before (with vehicle control) and after treatment with Cytochalasin D. For panels C,D, each dot represents the mean±s.d. for a single mouse, averaged over 2–3 imaging positions per mouse, representing seven before/after experiments from four different mice. (E) Scatter plot of the correlation length versus RMS velocity. Squares indicate before addition of cytochalsin D (with vehicle control), and circles represent after addition of cytochalasin D. The combined data were fit with a power-law function, yielding an exponent of α=−2.56 (blue line). Each dot represents the mean±s.e.m. for a single mouse, averaged over 2–3 imaging positions per mouse, representing seven before/after experiments from four different mice.

using PIV (Fig. S5A). We found no overall change in migration dynamics before or after treatment with these cell division inhibitors by either PIV or manual tracking (Fig. S5B–D). The decrease in division rates after addition of the inhibitors was not consistent in all cases (Fig. S5E). Across all mitotic inhibitor treatment conditions and controls, we found no correlation between the division rate and migration speed (Fig. S5F), suggesting that division rate does not affect cell migration in the tumor core.

DISCUSSION
Our work aimed to decipher cancer cell migration in the tumor core with single-cell resolution, using a physiological spontaneous cancer model. To address this, we used a pipeline to image tumor explants from spontaneously forming tumors in real time using long-term two-photon microscopy. We found that cells in the tumor core are remarkably dynamic. Cancer cells exhibited collective behaviors, such as coordinated migration, streaming and vortex-like movements. Coordinated migration was interspaced by brief pauses. Interestingly, there was no requirement for pausing during division, suggesting that dividing cells continue to flow with their neighbors. Finally, our results using pharmacological inhibitors suggest that migration in the tumor core is actively driven by the actin

cytoskeleton. The inverse relationship between speed and correlation length observed with cytochalasin D treatment is reminiscent of tissues close to a jamming transition (Angelini et al., 2011; Garcia et al., 2015); jamming transitions have recently been linked to cancer progression and tumor cell escape (Park et al., 2016; Oswald et al., 2017; Atia et al., 2018).

We speculate that the coordinated nature of tumor cell migration in our model is responsible for the migratory behavior we observed during cell division. Previous work in single migrating cells in vitro has led to the assumption that in order to divide, cells must first stop migrating (Abercrombie et al., 1970). However, in a densely packed tissue, as we observe in the tumor core, dividing cells can continue to migrate during division, probably because they are dragged by neighboring cells in the tissue, as previously suggested by intravital imaging of invading fibrosarcoma xenografts (Alexander et al., 2013). Our data suggest that this can also occur in the core of epithelial tumors. Our analysis regarding the influence of local collagen bundle orientation does not suggest any influence of these structures in 2D cell migration in the tumor core. However, the role of ECM in cell migration remains an active line of research and should be addressed in more depth in future studies, in particular the intersection of cell–ECM interactions and collective behavior between cells in 3D.

Tumor explant imaging provides a bridge between 3D *in vitro* invasion assays and intravital studies in living mice. On the one hand, embedding cancer cells in various 3D extracellular matrices allows for deciphering interactions with specific matrix components and molecular pathways involved in 3D migration. On the other hand, intravital imaging reveals cell dynamics in intact tissue, but xenografted tumors are not surrounded by a native stroma that co-evolves with the tumor, and thus they lack a truly disease-relevant microenvironment. The core of spontaneously developing tumors contains ECM that has co-evolved with the tumor, and therefore the influence of the structure of collagen on tumor cell migration can be addressed. Imaging of spontaneous cancer models allows for a better understanding of the co-adaptation of cancer cells to their native microenvironment.

We validated the robustness of our explant imaging model by comparing characteristic features of the explants to tumors *in vivo*. However, because tumors are resected from mice, some physiological features found *in vivo* were not recapitulated in our model. Intravital studies have suggested an enhanced migratory phenotype in proximity to blood vessels (Kedrin et al., 2008). In our system blood perfusion was abolished, so the contribution of the vasculature to tumor cell migration cannot be addressed. Another potential disadvantage of this system is the required use of 95% oxygen during culture. Tumors are often hypoxic (Höckel and Vaupel, 2001), whereas the surface layer of our tissue slices is exposed to hyperoxic conditions. However, oxygen diffusion is highly tissue-specific, and the amount of oxygen deeper in the tissue – where imaging was performed in this study – can be severely limited (Ivanova and Simeonov, 2012). We indeed measured a decrease of HIF1α, a hypoxia marker, indicating that hypoxic conditions were not maintained (Fig. S2E), suggesting that tumor explant culturing pipeline is probably not suitable for analysis of hypoxia-dependent cell behaviors. Nevertheless, these factors did not appear to affect tumor cell morphology, proliferation rates or migration speeds, all of which were stable over long imaging periods and fell within the range of migration speeds observed in intravital studies.

Our results suggest that migration in the tumor core is actively driven by the actin cytoskeleton. This prompts a number of questions related to the mechanisms of migration in the tumor core. First, what actin cytoskeleton regulators are involved in this migration? Do these cells have active protrusions, and what is the nature of these protrusions? Why does myosin-2 appear to play a limited role in migration? Do cells migrate directly along neighboring cells, or do cells secrete ECM at their interfaces, allowing for increased adhesion and migration? How do cell–cell adhesions coordinate both tight cell–cell contacts and migration? Regarding the consequences of tumor core migration, can these motile cells intravasate directly into the vasculature in the core and metastasize, without ever leaving the bulk of the tumor or migrating through the stromal-rich adjacent tissue? Although the spontaneous tumor model presented in this study offers many advantages to answering these questions, other models to study tumor core behavior will also be required for this future work.

Our tumor explant model opens new avenues for studying the behavior and dynamics of cells in the tumor core. Because vascular escape of cancer cells can also occur in deep regions of tumors, and not only at the invasive front (Deryugina and Kiosses, 2017), our work provides new insight into the nature of cell behavior in the tumor core prior to escape, which can lead to later metastasis, and represents a new, more physiological model for studying these collective cell behaviors in cancer. More broadly, our model will be an important tool to better understand collective cell behavior in tumors as well as cancer progression.

MATERIALS AND METHODS

Mice

All experiments were conducted in accordance with the guidelines of European Directive 2010/63/EU and national regulation for the protection of vertebrate animals used for experimental purposes (Decree 2013-118). All mice were kept in the Institut Curie Specific Pathogen Free (SPF) animal house for breeding.

In order to obtain the NICD/p53$^{-/-}$ mice (pVillin-CreER^{T2}; LSL-NICD-nGFP; p53$^{F/F}$) and NICD/Tom/p53$^{-/-}$ mice (pVillin-CreER^{T2}; LSL-NICD-nGFP; mT/mG; p53$^{F/F}$), previously described mice were crossed: the pVillin-CreER^{T2} mice (El Marjou et al., 2004), p53$^{F/F}$ mice (Jonkers et al., 2001), Rosa26-mT/mG mice (Muzumdar et al., 2007) and Rosa26-N1ic mice, referred to as NICD (Murtaugh et al., 2003). Rosa26-mT/mG mice express a membrane-targeted tandem dimer Tomato (mT) prior to Cre-mediated excision and a membrane-targeted EGFP (mG) following excision (Muzumdar et al., 2007). Membrane targeting was achieved using the MARCKS membrane tag (Muzumdar et al., 2007). Four-week-old mice were injected intraperitoneally with tamoxifen (1 mg/day) for five consecutive days. Eight months after tamoxifen injection, mice spontaneously develop invasive intestinal carcinoma as described in Chanrion et al. (2014). Mice used in this study were ∼80% female.

Tumor explant culture

A piece of intestine containing a tumor was isolated from a NICD/p53$^{-/-}$ mouse. The intestinal explant was flushed with PBS containing 2% antibiotic-antimycotic (Life Technologies), and cut into 4-mm pieces using a scalpel. The tumor pieces were then embedded in 4% (wt/vol) low melting point agarose (Life Technologies) in pre-warmed Leibovitz's L-15 medium. The agarose block containing the tumor pieces was sliced using a vibratome (Leica VT1000S), to 250 μm or 360 μm slices at a speed of 0.125 mm/s and a vibration frequency of 70 Hz. Imaging was performed at ∼60 μm away from the underlying filter, unless otherwise specified.

The tumor slices were deposited onto a cell culture filter (Millicell, 30 mm diameter, pore size 0,4 μm, Merck Millipore) and cultured at the air–liquid interface in a 35 mm tissue culture dish (FluoroDish, World Precision Instruments). Culture medium was DMEM-GlutaMAX (Gibco), supplemented with 1% antibiotic-antimycotic (Life Technologies), 2,5% fetal bovine serum, 0.25 U/ml insulin (Sigma-Aldrich), 100 μg/ml transferrin (Holo, Human Plasma, Calbiochem) and 10 ng/ml epidermal growth factor (Peprotech).

Time-lapse image acquisition

Tissue explants were maintained at 37°C in the microscope stage-top incubator (Okolab), in 95% O$_2$, 5% CO$_2$, 95% humidity. The explant was imaged using two-photon excitation microscopy on an inverted Leica SP8 microscope coupled to a femtosecond Chameleon Vision II laser (680–1350 nm; Coherent, Inc.), using a Leica 25×/0.95NA water immersion objective.

Three non-descanned Leica hybrid detectors were used, with the following filters: 525/25 nm (GFP), 575/25 (Tomato) and <492 nm (second-harmonic generation, SHG). The excitation wavelength was 960 nm for GFP and Tomato, and SHG was obtained at a wavelength of 910 nm.

Images were recorded every 15–30 min up to 40 h. 3D stacks were obtained at a step size of 0.5–2 μm intervals.

For the analysis of tumor cell migration, we used a total of six NICD/p53$^{-/-}$ mice, with one tumor explant being used for imaging per mouse. One tumor was excluded due to atypical tumor morphology (stromal dominant, few tumor cell-rich areas). Several positions were acquired per tumor explant, among which seven positions where retained for our study. From these seven positions, 14 z-slices were selected for manual tracking in 2D. A total of 685 cell trajectories were analyzed for the dynamics studies in Fig. 2 and Fig. 5, 857 cells for the directional correlation in Fig. 4C, 423 cells (3 mice) were used for the study of cell migration with respect to collagen (Fig. S3H–L) and 36 division events (3 mice) were used in Fig. 3C–E.

For treatment of the tumor explants with drug inhibitors, tumor explants were first imaged in the presence of vehicle control in the medium. After 6 h of imaging, medium was replaced and inhibitors added in the desired concentrations. Tumor explants were imaged for an additional 6 h in the

presence of inhibitors. Inhibitors used were the following: cytochalasin D (in DMSO, Sigma-Aldrich), para-nitroblebbistatin (in DMSO, Optopharma), CK-666 (in DMSO, Sigma-Aldrich), hydroxyurea (Sigma-Aldrich), mitomycin C (in PBS, Roche).

Image analysis

Z-stacks were processed using ImageJ (NIH). All images were corrected for brightness and contrast using the ImageJ software. 3D registration was performed using the 'Correct 3D Drift' plugin (Parslow et al., 2014). Rigid body registration (Correct 3D Drift) did not differ in terms of population-level cell dynamics when affine registration was added using collagen structures as a reference channel. For tracking, a random population of cells was selected without prior knowledge of their migration. These nuclei were then manually tracked in 2D using the MTrackJ plugin (Meijering et al., 2012). Tracking of large numbers of cells in 3D was not feasible as the high crowding of cancer cells in the tumor core does not allow for accurate segmentation. To obtain a large field of view (Fig. 1A), z-projected 3D stacks were stitched using the Grid/Stitching plugin (Preibisch et al., 2009) following flat-field correction after determining intensity inhomogeneity through imaging a uniform fluorescent field. For drug treatment experiments, cells were tracked for 200–400 min following addition of vehicle/drug to ensure stability of the tissue for quantification.

Analysis of migration trajectories

Following manual tracking of cell nuclei, cell trajectories were analyzed using custom analysis software written in Python (www.python.org) using the Numpy, Scipy and Matplotlib packages. Migration persistence was defined as the final displacement of a cell divided by the total trajectory length. MSD was determined using a Fast Fourier Transform based on the algorithm in (Calandrini et al., 2011). To determine directional correlation, for a given time-lapse image, all possible combinations of cells were determined for a given time-lapse movie. Directional correlation, defined as $\cos(\theta_{i,t}-\theta_{j,t})$ between two cells (designated i and j) was calculated for overlapping time frames t to determine the mean correlation.

To generate kymographs, cell trajectories were projected onto one dimension and plotted against time. Pauses were defined as consecutive time periods of ≥ 30 min without detectable movement of the nucleus. For comparison of speeds in dividing cells, the period 'during division' was defined as the 45 min prior to the appearance of the daughter cell nuclei. For quantification of collagen displacement, kymographs were generated in ImageJ. For each kymograph, the mean displacement speed was determined from the time points where the displacement was maximal.

For the analysis of cell migration dynamics and collagen structures, a binary mask was generated from a time projection of 2D collagen images by Gaussian filtering, thresholding and removal of small objects. Local orientation was determined by a linear fit along each contour point. Local contour orientations were then extrapolated outside of the collagen regions by an initial nearest neighbor extrapolation to the pixel grid and subsequent smoothing of this grid (Gaussian kernel, $\sigma=10$ px). With the resulting smoothened contour orientations, we performed a second extrapolation outside of the collagen regions and smoothening (Gaussian kernel, $\sigma=20$ px). This procedure was optimized empirically to achieve an extrapolated grid that visually reflected the collagen contour orientation. We then overlaid the extrapolated collagen orientation grid with the manually tracked cell trajectories. To determine the angular difference between the collagen orientation and cell trajectory, we took the difference between the angle of the cell displacement vector (from start to end of the trajectory) and the extrapolated collagen orientation at the mean trajectory position. For the Rayleigh test of uniformity, the directional bias was rescaled to 360°. Custom image analysis software is available upon request.

PIV analysis

PIV analysis was performed using the OpenPIV (www.openpiv.net) package in Python, with a window size of 32×32 px^2 ($\sim29\times29$ µm^2) and window overlap of 16×16 px^2 ($\sim15\times15$ µm^2). To avoid tracking noisy pixels and to avoid cell-poor regions, a mask was generated based on a thresholded image of the cell nuclei. Only pixels within this mask were considered in the PIV

analysis. Spurious vectors were identified using cross-correlation signal-to-noise analysis. For Fig. 4D and Movie 3, noisy vectors within the mask region were replaced by a local mean interpolation. For speed and correlation analyses, noisy vectors were eliminated and not interpolated. Directional correlation versus distance for PIV data was determined using a radial cross-correlation function as described in Garcia et al. (2015), and correlation length (ζ_{vv}) was determined by fitting these curves with the exponential function $F(x)=\exp(-x/\zeta_{vv})$. Mean 2D cell density (6377.19±434.55 cells/mm^2, mean±s.d.) was calculated by segmenting nuclei-labeled images used for PIV analysis using ilastik image analysis software (Sommer et al., 2011) and dividing the number of nuclei by the area of masked cell-rich regions. Fitting and determination of correlation of ζ_{vv} versus root mean square (RMS) velocity was performed by means of linear regression using a log transform of the data [for$F(x)=\exp b\, x^{\alpha}$, $\log F(x)=\alpha\log x+b$, where α is the power law and b is a constant]. For analysis of migration with respect to collagen bundles, a similar approach was taken for comparing PIV data as for trajectories from manual tracking, where the angular difference was measured between each PIV vector and the extrapolated collagen orientation at the position of the vector, yielding essentially identical results as for manual tracking.

EdU incorporation study

For this study, NICD/p53$^{-/-}$ or NICD/Tom/p53$^{-/-}$ tumor-bearing mice were used. Three mice were intraperitoneally injected with 100 µm of EdU at 10 mM and euthanized 3 h later (in vivo EdU condition). Tumors were sliced and EdU incorporation was revealed using the Click-iT EdU Alexa Fluor 647 kit (Invitrogen). Six other mice were euthanized and tumors were sliced to 250-µm-thick slices using a vibratome (Leica VT1000S). Slices were incubated as described above and 10 µM EdU was added to the medium for hours 0–3 h or 21–24 h, with three mice per condition. Following incubation, EdU incorporation was revealed according to the manufacturer's instructions.

Immunofluorescence staining and image acquisition

In order to minimize tissue heterogeneity, staining at 0 h and at 24 h was performed on matched samples, where two 250-µm-thick adjacent tissue slices were used, one for the 0 h time point and the other for the 24 h time-point after incubation. 250-µm-thick tissue explant slices were embedded in OCT compound and sliced to 5-µm-thin cryosections. Immunofluorescence labeling was performed using the following antibodies: anti-E-cadherin (20 µg/ml, Life Technologies, 13-1900, lot 1412296A), anti-ZO-1 (5 µg/ml, EMD Millipore, MABT11, lot 2808214), anti-ZEB-1 (1:100, Bethyl Laboratories, IHC-00419), anti-α-SMA (1:200, Dako, M0851), anti-Ki-67 (2.5 µg/ml, Abcam, ab15580, lot GR192874-1) and anti-cleaved caspase-3 (1:100, Cell Signaling Technologies, 9661). F-actin was labeled using phalloidin (1:150, Alexa Fluor 633, Invitrogen, A22284) and DNA was detected using DAPI (1:500).

Immunofluorescence images were acquired using a Zeiss LSM880NLO inverted laser scanning confocal microscope equipped with spectral detection confocal head. We used laser lines 405, 488, 561 and 633 nm and the following objectives: 25×/0,8 OIL, W, Gly LD LCI PL APO (UV) VIS-IR, 40×/1.3 OIL DICII PL APO (UV) VIS-IR and 63×/1.4 OIL DICII PL APO. Images were processed using ImageJ.

Quantification of the percentage of cleaved caspase-3 areas

Stitched images of entire thin tissue slices ($\sim$3 mm×2 mm) were acquired using a Zeiss LSM880NLO inverted laser scanning confocal microscope (25×/0.8 OIL, W, Gly LD LCI PL APO (UV) VIS-IR objective) for DAPI and cleaved caspase-3 (CC3) channels. Stitching was performed using ZEN software (Carl Zeiss). Following z-projection, channels were filtered (Gaussian) and thresholded. The ratio of CC3 area to DAPI area was calculated for two separate slices from three different mice, at three different depths from the surface (0, 50 and 100 µm), at 0 h and after 24 h of culturing.

Western blot

Western blot analysis was performed for tumor tissue slices before and after a 24 h incubation in 95% O$_2$ and 5% CO$_2$ (imaging conditions) (Majmundar et al., 2010). Tissue slices where then snap-frozen and lysed using 50 mM Tris pH 6.8, 2% SDS, 5% glycerol, 2 mM DTT, 2.5 mM EDTA, 2.5 mM

EGTA, 4 mM Na$_3$VO$_4$, 20 mM NaF, 2× phosphatase and protease inhibitors cocktails (Sigma-Aldrich). Tissue lysis was performed using a Precellys homogenizer (Bertin Technologies), following manufacturer's instructions. Blots were incubated with primary antibodies (1:2000 rabbit anti-GAPDH, Sigma-Aldrich, G9545; 1:250 mouse anti-HIF1α, R&D Systems, MAB 1536) overnight at 4°C in 5% BSA, and detected using peroxidase-conjugated secondary antibodies (1:2500 goat anti-mouse Poly-HRP, Fisher Scientific, Cat. No. 10371084; and 1:5000 goat anti-rabbit Poly-HRP, Fisher Scientific, Cat. No. 10763265) for 1 h at room temperature.

Statistical analysis

Statistical analysis was performed using Python with the Numpy, Scipy, Matplotlib and Astropy packages, and GraphPad (Prism). The specific tests used are specified in the figure legends. Sample sizes were estimated to ensure population level characteristics within tumors and across different tumors given the heterogeneity observed in preliminary studies.

Competing interests

The authors declare no competing or financial interests.

Author contributions

Conceptualization: R.S., A.G.C., D.M.V.; Methodology: R.S., F.E.M., J.B., D.K.; Software: A.G.C.; Validation: R.S., A.G.C.; Formal analysis: R.S., A.G.C.; Investigation: R.S., J.B., S.R.; Writing - original draft: R.S., A.G.C., D.M.V., S.R.; Writing - review & editing: R.S., A.G.C., D.M.V.; Visualization: A.G.C., R.S.; Supervision: D.M.V.; Funding acquisition: D.M.V.

Supplementary information

Supplementary information available online at
http://jcs.biologists.org/lookup/doi/10.1242/jcs.220277.supplemental

References

Abercrombie, M., Heaysman, J. E. M. and Pegrum, S. M. and Pegrum, S. M. (1970). The locomotion of fibroblasts in culture II. "Ruffling". *Exp. Cell Res.* **60**, 437-444.

Alexander, S., Weigelin, B., Winkler, F. and Friedl, P. (2013). Preclinical intravital microscopy of the tumour-stroma interface: invasion, metastasis, and therapy response Intrinsic contrast. *Curr. Opin. Cell Biol.* **25**, 659-671.

Angelini, T. E., Hannezo, E., Trepat, X., Marquez, M., Fredberg, J. J. and Weitz, D. A. (2011). Glass-like dynamics of collective cell migration. *Proc. Natl. Acad. Sci. USA* **108**, 4714-4719.

Atia, L., Bi, D., Sharma, Y., Mitchel, J. A., Gweon, B., Koehler, S. A., Decamp, S. J., Lan, B., Kim, J. H., Hirsch, R. et al. (2018). Geometric constraints during epithelial jamming. *Nat. Phys.* **14**, 613-620.

Calandrini, V., Pellegrini, E., Calligari, P., Hinsen, K. and Kneller, G. R. (2011). nMoldyn - Interfacing spectroscopic experiments, molecular dynamics simulations and models for time correlation functions. *Collection SFN.* **12**, 201-232.

Chambers, A. F., Groom, A. C. and Macdonald, I. C. (2002). Dissemination and growth of cancer cells in metastatic sites. *Nat. Rev. Cancer* **2**, 563-572.

Chanrion, M., Kuperstein, I., Barrière, C., El Marjou, F., Cohen, D., Vignjevic, D., Stimmer, L., Paul-Gilloteaux, P., Bièche, I., Tavares, S. D. R. et al. (2014). Concomitant Notch activation and p53 deletion trigger epithelial-to-mesenchymal transition and metastasis in mouse gut. *Nat. Commun.* **5**, 5005.

Clark, A. G. and Vignjevic, D. M. (2015). Modes of cancer cell invasion and the role of the microenvironment. *Curr. Opin. Cell Biol.* **36**, 13-22.

Deryugina, E. I. and Kiosses, W. B. (2017). Intratumoral cancer cell intravasation can occur independent of invasion into the adjacent stroma article intratumoral cancer cell intravasation can occur independent of invasion into the adjacent stroma. *Cell Rep.* **19**, 601-616.

El Marjou, F., Janssen, K.-P., Hung-Junn Chang, B., Li, M., Hindie, V., Chan, L., Louvard, D., Chambon, P., Metzger, D. and Robine, S. (2004). Tissue-specific and inducible Cre-mediated recombination in the gut epithelium. *Genesis* **39**, 186-193.

Friedl, P. and Wolf, K. (2010). Plasticity of cell migration: a multiscale tuning model. *J. Cell Biol.* **188**, 11-19.

Garcia, S., Hannezo, E., Elgeti, J., Joanny, J.-F., Silberzan, P. and Gov, N. S. (2015). Physics of active jamming during collective cellular motion in a monolayer. *Proc. Natl Acad. Sci. USA* **112**, 15314-15319.

Gligorijevic, B., Bergman, A. and Condeelis, J. (2014). Multiparametric classification links tumor microenvironments with tumor cell phenotype. *PLoS Biol.* **12**, e1001995.

Höckel, M. and Vaupel, P. (2001). Tumor hypoxia: definitions and current clinical, biologic, and molecular aspects. *J. Natl. Cancer Inst.* **93**, 266-276.

Ivanova, R. and Simeonov, G. (2012). A formula for the oxygen uptake of thin tissue slice in terms of its surface oxygen tension. *Comput. Math. Appl.* **64**, 322-336.

Jonkers, J., Meuwissen, R., Van Der Gulden, H., Peterse, H., Van Der Valk, M. and Berns, A. (2001). Synergistic tumor suppressor activity of BRCA2 and p53 in a conditional mouse. *Nat. Genet.* **29**, 418-425.

Kedrin, D., Gligorijevic, B., Wyckoff, J., Verkhusha, V. V., Condeelis, J., Segall, J. E. and Van Rheenen, J. (2008). Intravital imaging of metastatic behavior through a mammary imaging window. *Nat. Methods* **5**, 1019-1021.

Lambert, A. W., Pattabiraman, D. R. and Weinberg, R. A. (2017). Emerging biological principles of metastasis. *Cell* **168**, 670-691.

Majmundar, A. J., Wong, W. J. and Simon, M. C. (2010). Hypoxia-inducible factors and the response to hypoxic stress. *Mol. Cell* **40**, 294-309.

Meijering, E., Dzyubachyk, O. and Smal, I. (2012). Methods for cell and particle tracking. *Methods Enzymol.* **504**, 183-200.

Murtaugh, L. C. stanger, B. Z., Kwan, K. M. and Melton, D. A. (2003). Notch signaling controls multiple steps of pancreatic differentiation. *Proc. Natl. Acad. Sci. USA* **100**, 14920-14925.

Muzumdar, M. D., Tasic, B., Miyamichi, K., Li, L. and Luo, L. (2007). A global double-fluorescent Cre reporter mouse. *Genesis* **45**, 593-605.

Oswald, L., Grosser, S., Smith, D. M. and Käs, J. A. (2017). Jamming transitions in cancer. *J. Phys. D Appl. Phys.* **50**, 483001.

Park, J.-A., Atia, L., Mitchel, J. A., Fredberg, J. J. and Butler, J. P. (2016). Collective migration and cell jamming in asthma, cancer and development. *J. Cell Sci.* **129**, 3375-3383.

Parslow, A., Cardona, A. and Bryson-Richardson, R. J. (2014). Sample drift correction following 4D confocal time-lapse imaging. *J. Vis. Exp.* **86**, e51086.

Patsialou, A., Bravo-Cordero, J. J., Wang, Y., Entenberg, D., Liu, H., Clarke, M. and Condeelis, J. S. (2013). Intravital multiphoton imaging reveals multicellular streaming as a crucial component of in vivo cell migration in human breast tumors. *IntraVital* **2**, e25294.

Prall, F. (2007). Tumour budding in colorectal carcinoma. *Histopathology* **50**, 151-162.

Preibisch, S., Saalfeld, S. and Tomancak, P. (2009). Globally optimal stitching of tiled 3D microscopic image acquisitions. *Bioinformatics* **25**, 1463-1465.

Provenzano, P. P., Eliceiri, K. W., Campbell, J. M., Inman, D. R., White, J. G. and Keely, P. J. (2006). Collagen reorganization at the tumor-stromal interface facilitates local invasion. *BMC Med.* **4**, 38.

Provenzano, P. P., Inman, D. R., Eliceiri, K. W., Knittel, J. G., Yan, L., Rueden, C. T., White, J. G. and Keely, P. J. (2008). Collagen density promotes mammary tumor initiation and progression. *BMC Med.* **6**, 11.

Staneva, R., Barbazan, J., Simon, A., Vignjevic, D. M. and Krndija, D. (2018). Cell migration in tissues: explant culture and live imaging. *Methods Mol. Biol.* **1749**, 163-173.

Sommer, C., Strähle, C., Köthe, U. and Hamprecht, F. A. (2011). ilastik: Interactive Learning and Segmentation Toolkit. pp. 230-233. Proceedings of the International Symposium on Biomedical Imaging (ISBI). doi: 10.1109/ISBI.2011. 5872394

Tambe, D. T., Corey Hardin, C., Angelini, T. E., Rajendran, K., Park, C. Y., Serra-Picamal, X., Zhou, E. H., Zaman, M. H., Butler, J. P., Weitz, D. A. et al. (2011). Collective cell guidance by cooperative intercellular forces. *Nat. Mater.* **10**, 469-475.

Vignjevic, D., Schoumacher, M., Gavert, N., Janssen, K.-P., Jih, G., Laé, M., Louvard, D., Ben-Ze'ev, A. and Robine, S. (2007). Fascin, a novel target of β-catenin-TCF signaling, is expressed at the invasive front of human colon cancer. *Cancer Res.* **67**, 6844-6853.

Weigelin, B., Bakker, G.-J. and Friedl, P. (2012). Intravital third harmonic generation microscopy of collective melanoma cell invasion. *IntraVital* **1**, 32-43.